frontiers | Frontiers in Mechanical Engineering

TYPE Original Research
PUBLISHED 30 October 2024
DOI 10.3389/fmech.2024.1410743

OPEN ACCESS

EDITED BY
Libor Pekař,
Tomas Bata University in Zlín, Czechia

REVIEWED BY
Arash Shams Taleghani,
Ministry of Science, Research and Technology, Tehran, Iran
Abdelmjid Qadi El Idrissi,
Hassan Premier University, Morocco

*CORRESPONDENCE
Karla Gonçalves,
karlag@fe.up.pt

RECEIVED 01 April 2024
ACCEPTED 21 October 2024
PUBLISHED 30 October 2024

CITATION
Gonçalves K, Varga S, Butrymowicz D and Śmierciew K (2024) Analysis of HEM applicability for a subcritical flashing ejector at low motive pressure.
Front. Mech. Eng. 10:1410743.
doi: 10.3389/fmech.2024.1410743

Analysis of HEM applicability for a subcritical flashing ejector at low motive pressure

Karla Gonçalves[1]*, Szabolcs Varga[1], Dariusz Butrymowicz[2] and Kamil Śmierciew[2]

[1]INEGI—Institute of Science and Innovation in Mechanical and Industrial Engineering, Faculty of Engineering Campus, Porto, Portugal, [2]Department of Thermal Engineering, Białystok University of Technology, Białystok, Poland

Validated CO_2 ejector models are essential for developing high-performance refrigeration and heat pump cycles. This study focuses on assessing the Homogeneous Equilibrium Model's applicability to simulate a CO_2 flashing ejector at a reduced pressure of 0.47. The model was implemented in FLUENT, integrating a user-defined real gas model. Simulation results with different boundary condition options were compared to experimental data. The analysis was carried out to evaluate the predictive capabilities of the model and assess the experimental data quality. The results indicate that the developed model accurately estimated the motive mass flow rate, with a maximum relative error of 5.7%, showing better performance than previously reported data. The entrained flow rate, assuming double choking operation, was significantly higher than the experimental measurement, and the CFD-predicted wall static pressure underestimated the experimental profile, suggesting single-choked ejector operation. In contrast, the outflow density was better predicted under the same assumption, with an average error of 8.6%. Nevertheless, the simulated temperature profiles showed good agreement with the experimental data, especially when using the experimental entrained mass flow rate as a boundary condition.

KEYWORDS

two-phase ejector, CFD modeling, experimental data, low motive pressure, R744

1 Introduction

Carbon dioxide (CO_2) based refrigeration and heat pump cycles are becoming more widely deployed in recent years, due to a number of interesting characteristics of CO_2 including high volumetric heat capacity, excellent transport properties, availability and low impact on the environment. Despite its potential as a refrigerant, using CO_2 presents certain challenges, including a relatively poor system energy performance in a single-stage compression system when compared to using synthetic working fluids. In order to overcome this problem, innovative cycles with alternative configurations have been studied. One promising solution is to integrate a flashing ejector into the CO_2 cycle for partial expansion work recovery. An ejector is a simple device often used to compress a low-pressure fluid to a higher-pressure using heat as the energy source, without using a mechanical compressor. Besides refrigeration (Palacz et al., 2015), this solution has been also studied for other industrial applications, such as carbon capture (Reddick et al., 2016), desalination (Sharifi et al., 2021), power generation and chemical processing (Parikhani et al., 2021).

The general operating principle of CO_2 ejectors is known and it can be found in the literature, e.g., in Hassanain et al. (2015), Ringstad et al. (2020) and Liu et al. (2022). Despite the significant interest, a comprehensive understanding and an accurate mathematical description of the underlying physics is yet to be achieved through experimental and numerical investigations (Giacomelli, Mazzelli, et al., 2019). The flow behaviour within these devices is complex, particularly regarding the mass, momentum and energy exchange between the inlet streams. For two-phase ejectors, the complexity increases due to non-equilibrium states induced by thermodynamic and transport non-equilibria. For more details on two-phase flow modelling, the reader is referred to (Ishii and Hibiki, 2006; Banasiak and Hafner, 2011). Thermodynamic non-equilibrium is associated with the superheated or subcooled condition of a gas or liquid, while transport non-equilibrium pertains to differences in temperature, pressure, velocity between phases and chemical potential (Ringstad et al., 2020). The expansion process in the motive nozzle is a non-equilibrium process, representing one of the most challenging aspects of modelling CO_2 ejectors (Ringstad et al., 2020). To address these effects, multiphase models are utilized, in which the interaction between different phases is mathematically described based on predefined assumptions. The available models for ejector flow simulation can be classified into two major groups: 1) the two-fluid approach, where separate sets of equations are solved for each phase (Sharifi et al., 2021) and 2) the pseudo-fluid approach, where a single set of equations is solved, considering the average properties of all phases (Colarossi et al., 2012).

The Two-Fluid Model (TFM) incorporates separate momentum equations for each phase, accounting for non-equilibrium between the phases with separate velocity vector fields (Ishii and Hibiki, 2006). However, due to the interdependence of the phases, the TFM requires multiple closure models for accurate solutions. The application of the TFM to simulate two-phase ejectors is relatively recent. Ringstad and Hafner (2020) published a TFM specifically designed for R744 two-phase ejectors. This model incorporates non-equilibrium states related to temperature, momentum, and chemical potential. Considering the model complexity and computational cost, the authors concluded that TFM may not compensate for the increased effort when compared to simpler models, such as the Homogeneous Equilibrium Model, with increased accuracy. The average error in mass flow rate prediction for the studied operating conditions is similar between the two models. Nevertheless, there is a potential for enhancing the physical realism and overall simulation accuracy by integrating and improving the closure models (Ringstad and Hafner, 2020).

An alternative approach to model complex fluid flows is represented by the Lattice Boltzmann method (LBM). It is based on a micro or mesoscopic perspective, which may result in some advantages over its macroscopic alternatives, such as the TFM. LBM directly captures interfaces between the fluid phases, eliminating the need for slip boundary conditions (Noori et al., 2019). LBM is often applied to fully resolved multiphase flows involving small droplets and bubbles (Huang et al., 2013), which does not apply to two-phase flow ejectors. It may offer valuable insights into flashing nozzle flows by enabling a detailed examination of condensation processes or coalescence phenomena, but it has not yet been addressed. For further details on LBM, see Noori et al. (2019) and Taleghani and Noori (2022).

The pseudo-fluid approaches can be classified into two groups based on the treatment of thermodynamic equilibrium (Ringstad et al., 2020): (1) models that assume thermodynamic equilibrium and (2) models that incorporate thermodynamic non-equilibrium. The best known Homogeneous Equilibrium Model (HEM) belongs to the first group assuming thermodynamic equilibrium between the phases at all points (Banasiak and Hafner, 2011). This implies that both phases are characterized by the same temperature and pressure. Additionally, HEM considers perfect mixing of the phases, thus the flow can be described with an identical velocity and pressure field (Angielczyk et al., 2019). The HEM approach can be extended to consider thermodynamic non-equilibrium by introducing a finite relaxation time (Zheng et al., 2022). This model is known as the Homogeneous Relaxation Model (HRM). HRM uses an empirical relaxation time constant, specific to each ejector. Haida et al. (2018) studied the choice relaxation time constant to obtain accurate results for different operating regimes of the CO_2 ejector nozzle. Compared with HEM, the authors obtained similar accuracy for the motive mass flow rate prediction when the operating pressure was higher than 5.9 MPa. For lower pressures, the HRM led to more accurate results. Further studies on the application of HRM in ejector flow can be found in Colarossi et al. (2012), Palacz et al. (2017) and Bodys et al. (2022).

Another pseudo-fluid approach considering thermodynamic non-equilibrium is the mixture model. In this case, the thermodynamic properties of the mixture (phases) are calculated as mass-weighted average values. Giacomelli et al. (2019) developed a mixture model and compared the results with the HEM for simulating a CO_2 flashing ejector. The authors found that the mixture model exhibits poorer and slower convergence and similar accuracy in predicting the axial pressure profile inside the ejector. However, the mixture model demonstrated superior accuracy in predicting the ratio between the secondary and primary mass flow rate (entrainment ratio) and motive mass flow rate. The mixture model required approximately ten times more computational effort than the HEM. Moreover, the lack of comprehensive literature data has hindered the performance of low dynamic pressure testing and validation (Zheng et al., 2022).

Based on the literature review, it can be concluded that although alternative models to HEM may offer better accuracy under specific flow conditions, they often require prior calibration and/or increased time and computational resources. Besides, literature data has demonstrated that the HEM applied in CO_2 flashing ejectors yields reasonably good results when compared with experimental data. Lucas et al. (2014) developed an HEM approach in the OpenFOAM software. The ejector flow was simulated by varying parameters such as primary and secondary inlet pressures and enthalpies. The results were compared with experimental data and according to the authors, a good agreement was obtained for the ejector pressure profile without a suction flow. Similarly, Fang et al. (2019) and Smolka et al. (2013) obtained good agreement between numerical predictions with experimental data for pressure profiles. HEM can accurately predict the entrainment ratio (ER) for motive inlet pressures higher than the critical point. Liu et al. (2022) obtained a maximum simulation error of 6.25% (with an average error of

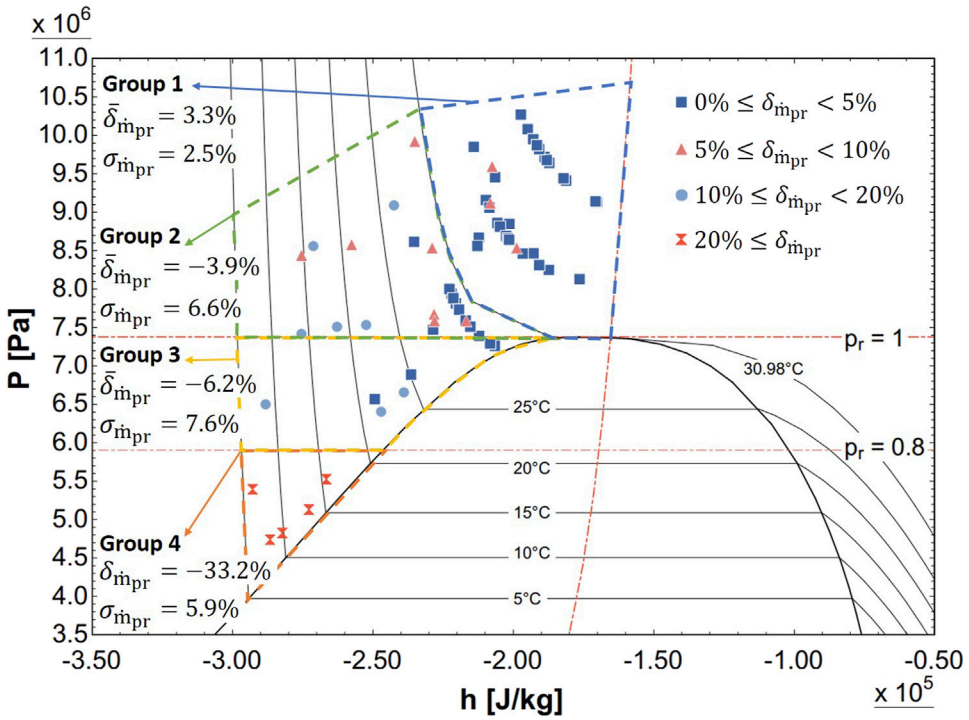

FIGURE 1
Motive mass flow rate prediction errors as a function of the primary flow inlet properties based on the results in Smolka et al. (2013), Lucas et al. (2014), and Palacz et al. (2015).

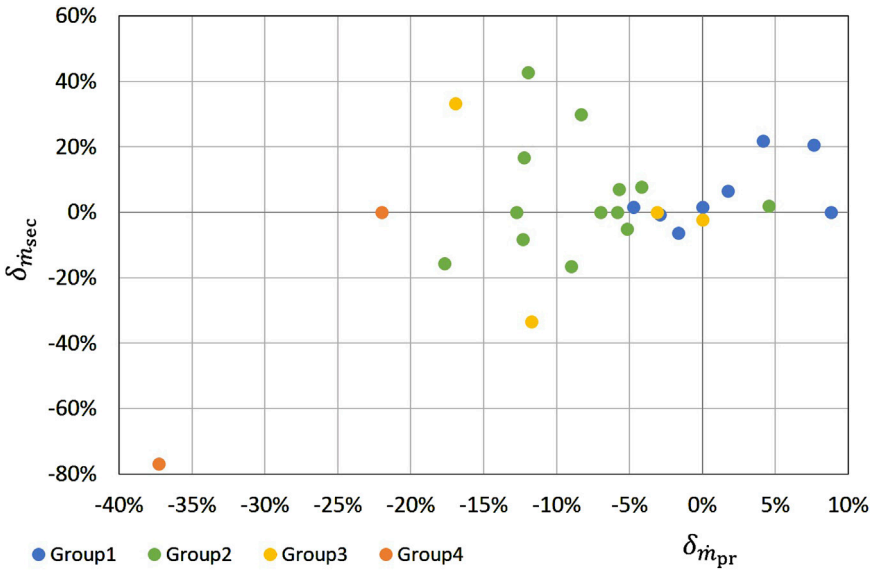

FIGURE 2
Secondary vs. primary mass flow rate prediction errors by Smolka et al. (2013) and Palacz et al. (2015), coloured by primary inlet conditions groups.

2%) for the entrainment ratio under transcritical operating conditions.

A comprehensive model validation analysis was carried out for the primary mass flow ($\dot{m}_{pr}$) rate under various operating conditions by Smolka et al. (2013), Lucas et al. (2014) and Palacz et al. (2015). The results are summarized in Figure 1, indicating the primary inlet conditions (enthalpy and pressure) and the relative prediction error levels ($\delta_{\dot{m}_{pr}}$). The results were analysed according to reduced properties. The reduced temperatures (T_r) and pressures (p_r) were obtained by dividing the actual values by the values at the

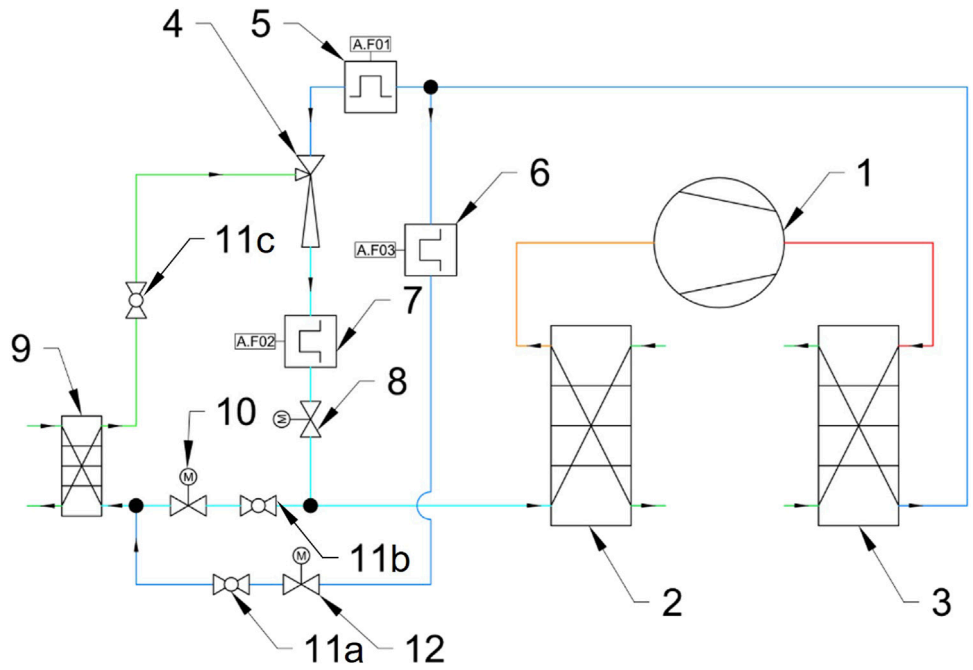

FIGURE 3
Simplified diagram of the ejector test rig.

critical point for the specific working fluid. Four different groups were identified: Group 1 T_r and p_r are higher than 1 (supercritical state), Group 2 only p_r is higher than 1, Group 3 considers $1< p_r \leq 0.8$ and Group 4 is for p_r inferior to 0.8. It was observed that the model performs best for Groups 1 and 2. Within Group 2, the HEM performance improved as T_r increased. The highest error in predicting the motive mass flow rate was found within the conditions in Group 4, with an average error ($\bar{\delta}_{\dot{m}_{pr}}$) of −33.2%. The authors concluded that HEM exhibits superior performance in predicting the primary mass flow rate when the fluid properties at the ejector inlet are in the supercritical or near supercritical range.

Simulated secondary flow rate ($\dot{m}_{sec}$) data using HEM in comparison to experimental results can be found in Smolka et al. (2013) and Palacz et al. (2015). Figure 2 illustrates the simulation for the error secondary mass flow rate as a function of $\delta_{\dot{m}_{pr}}$ for the same data groups identified in Figure 1. Looking at Figure 2, one may not find a clear error pattern regarding the developed HEM prediction capability for the primary and secondary flows. Nevertheless, when the prediction error is low for $\dot{m}_{pr}$, $\dot{m}_{sec}$ simulation tended to be also accurate. Additionally, when the primary mass flow rate was over-predicted, the secondary mass flow rate tended to be over-predicted too.

Literature data indicates that HEM is capable of accurately simulating two-phase ejectors when the fluid at the primary inlet is in supercritical conditions. However, when the ejector operates at lower inlet pressures ($p_r < 0.8$), the applicability of the model is less explored, especially in the case when the ejector operates under off-design conditions. The necessity of this research arises from the existing gap in understanding, as investigating the model's performance under low-pressure conditions is crucial for improving the prediction of ejector efficiency. The main objective of this work is to assess the HEM's applicability for a flashing ejector operating under relatively primary inlet pressure conditions. The presented study involves a comprehensive analysis of the predicted flow profile, predicted fluid properties at the ejector inlets and outlet and predicted mass flow rates, in comparison to experimental data. Additionally, different types of boundary conditions are evaluated to qualitatively assess the measured experimental data. This work expands the understanding and application of HEM for Non-equilibrium states can originate from thermodynamic and transport non-equilibria reduced primary inlet pressures below 0.8, which may contribute to ejector technology progress.

2 Methodology

2.1 Experimental setup

The measurements were carried out with an ejector test rig using CO_2 as the working fluid. Figures 3, 4 illustrate a diagram and photos of the experimental setup, respectively. The condenser (3) supplies liquid CO_2 to the ejector (4) nozzle with the primary mass flow, while the entrained vapour comes from the evaporator (9). The outlet pressure of the ejector (p_{out}) was controlled by an electronic expansion valve (8). The mixed stream from the ejector outlet was directed to a second evaporator (2), by maintaining the ball valve (11b) closed during the experimental runs. The purpose of this evaporator was to make sure that the CO_2 at the compressor inlet was in the vapour phase. Valves (11a) and (11c) remained open during the experimental runs. The vapour pressure was increased by the compressor (1) before entering the condenser (3). The amount of CO_2 flowing into the evaporator (9) was regulated by a throttling valve (12) and monitored by a flow meter (6).

FIGURE 4
Photo of the test rig.

The temperature was measured using calibrated type T-thermocouples, with an error of approximately ±0.4 K. The deviations between the thermocouple readings after calibration did not exceed ±0.1 K. For the ejector temperature profile, the sensors were mounted in sleeves and positioned perpendicular to the stream within the ejector interior. The remaining temperature sensors were installed in the pipeline walls.

The pressure was measured using pressure transducers (WIKA S-10) with a range of 1,000 psi (i.e. 6.89 MPa) and an accuracy of 0.25% on a full scale. Density and flow rates were measured using Endress + Hauser Coriolis mass flow meters with a maximum measurement uncertainty of 0.1% for liquids and 0.5% for gases for the mass flow rate, and ±0.5 kg/m^3 for liquid density.

The properties of the motive flow, such as pressure (p_{pr}) and temperature (T_{pr}), were measured immediately before the inlet of the motive chamber, while the pressure (p_{sec}) and temperature (T_{sec}) of the entrained flow were assessed inside the suction chamber. On the motive flow side, a flow meter (5) was installed to determine the corresponding flow density (ρ_{pr}) and mass flow rate ($\dot{m}_{pr}$). Another flow meter was positioned on the pipe branch connecting the condenser outlet to the evaporator inlet (6) to measure the entrained flow rate ($\dot{m}_{sec}$). Performing the entrained mass flow rate measurement in the liquid line prevents the flow meter from generating flow resistance at the vapour inlet. The sensor indicated by number (7) was used to measure the fluid density at the ejector discharge pipeline (ρ_{out}).

2.2 Ejector geometry

The ejector used in the experiments was a two-phase flashing ejector, which was not specifically designed for the present study. Its main geometrical features are indicated in Figure 5. It was designed such that a fine adjustment of the drive nozzle exit position relative to the constant area section could be done by a spacer. The diameter of the mixing chamber could also be changed by inserting a sleeve of known thickness into the mixing chamber. This design feature enhanced the flexibility of the ejector setup. The experimental tests reported in this work were carried out for an ejector with a baseline mixing chamber diameter of 4 mm and a modified diameter of 3 mm. The nozzle exit position was set to 4 mm from the constant are section inlet. The locations of pressure and temperature sensors within the ejector body are identified in Figure 5 by numbers 1–7.

2.3 Critical analysis of the experimental results

Three experimental points (Run 1–3) were considered for the current analysis. It is important to note that the double-choked ejector operation (choked primary and secondary streams) was not ensured during the test. Table 1 summarizes the results of the experimental tests for each run, and the results for the verification process.

To validate the experimental data points, EES (F-chart, United States) was used to compare the measured thermodynamic properties of CO_2 to the software's property functions. To identify a thermodynamic state, only two independent properties are needed. At the primary inlet, the CO_2 was in a subcooled liquid state, thus pressure, temperature and density can be considered independent properties. Any of these two can be used to verify the third one. Here, two approaches were implemented. In the first approach (A), cross-checking was carried out for the density using measured pressure and temperature data. In the second approach (B), the expected temperatures were evaluated with the experimentally measured pressure and density values. The results of this verification process are shown in Table 1. It can be seen from the table that the measured temperatures were considerably higher than the ones determined using EES with the experimental pressure and density values as inputs. The difference is about 9°C, which significantly exceeds the temperature measurement error. However, the difference can be justified by the sensor position, once this was installed in the pipeline wall. The difference between the measured and EES calculated densities is about 6% (≈55 kg/m^3) for each experimental condition. Therefore, it was assumed the uncertainty regarding the experimental determination of pressure and density was the lowest, thus these properties were used as boundary conditions on the primary inlet side for the ejector in the CFD model.

A different approach was used to verify the experimental data points obtained for the ejector outlet. The results can be found in Table 1. Such as before, pressure, temperature and density data were recorded, however, in this case, outlet temperature and pressure cannot be considered independent because CO_2 exits the ejector as a liquid-vapour mixture. Therefore, the verification process involved calculating the saturation temperature (T^*_{out}) corresponding to the

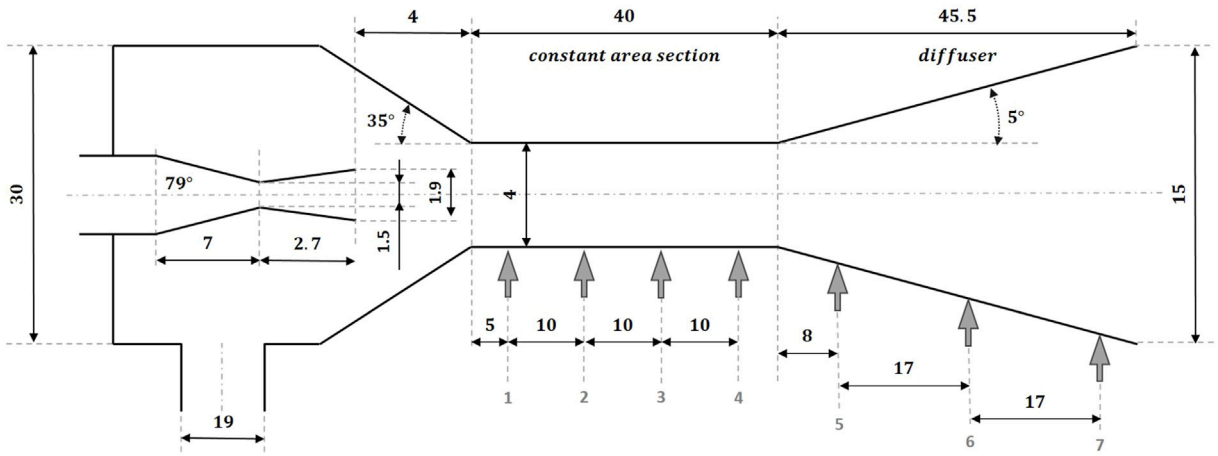

FIGURE 5
Ejector geometry detail in mm, with indication of the pressure and temperature sensors positions.

TABLE 1 Operating conditions and results obtained during the experimental test compared with the computed values.

	Experimental data				Computed values		
	p	T	ρ	ṁ	ρ* (p, T)	T* (p, ρ)	x* (p, ρ)
	[kPa]	[°C]	[kg/m³]	[g/s]	[kg/m³]	[°C]	—
Motive nozzle inlet (pr)	3,483	−1.4	992	71.1	937	−10.7	—
	3,474	−1.3	991	70.8	936	−10.5	—
	3,451	−2.1	995	74.0	941	−11.3	—
Suction chamber inlet (sec)	2,012	−4.9	—	0.522	—	—	—
	2,013	−4.3	—	0.409	—	—	—
	1,732	−6.6	—	1.23	—	—	—
Ejector outlet (out)	2,233	−8.9	292	—	55.7	−15.9#	0.153
	2,227	−8.4	288	—	55.3	−16.0#	0.155
	1,961	−10.3	204	—	47.7	−20.2#	0.213

*correspond to computed values using the property function of EES. #saturated temperature.

measured pressure (p_{out}). It was observed that T^*_{out} was significantly lower than the experimentally recorded temperature (T_{out}). For p_{out} and T_{out}, CO_2 would be in a superheated vapour state at the ejector outlet, which is unexpected. Therefore, these two measured properties cannot be simultaneously used to identify the fluid state at the ejector outlet. This is also indicated by determining the density (ρ^*_{out}) from the measured pressure (p_{out}) and temperature (T_{out}). The results were approximately 79% lower than the experimentally obtained data.

Because of the experimental error, it is evident that experimental p_{out}, ρ_{out} and T_{out} data could not be simultaneously used for model validation. Hence, it was important to evaluate which measured properties reflect the ejector outlet conditions more accurately. Generally, temperature is more difficult to measure with high accuracy compared to static pressure. Therefore, the vapour quality (x^*_{out}) was calculated for measured p_{out} with ρ_{out}, varying from 15% to 21% (see Table 1). These results are more realistic compared to data obtained for measured temperature (T_{out}) and pressure (p_{out}). It is important to acknowledge that the presence of any oil in the refrigerant fluid could introduce an uncertainty of up to 60 kg/m³ in the density measurement. This estimated level of uncertainty was also considered in the analysis confirming that the fluid left the ejector in a humid vapour state. Therefore, the discrepancy between the measured and expected (saturation) temperatures was attributed mostly to the uncertainty in the temperature sensing (location and measurement errors).

For any ejector, the following energy balance equation should apply when using experimentally measured data:

$$\dot{m}_{pr} \cdot h_{0,pr} + \dot{m}_{sec} \cdot h_{0,sec} = \dot{m}_{out} \cdot h_{0,out} + \Delta E. \quad (1)$$

The last term (ΔE) on the right-hand side includes a combination of the following two factors: i) measurement error and ii) heat transfer through the ejector wall (heat losses). The stagnation enthalpies in Equation 1 were determined using the

TABLE 2 Energy balance calculation and entrainment ratio (ER), using the experimental results.

	Measured		EES output			ΔE [W]	ER
	$\dot{m}_{pr}$ [g/s]	$\dot{m}_{sec}$ [g/s]	h^*_{pr} (p,ρ) [kJ/kg]	h^*_{sec} (p,T) [kJ/kg]	h^*_{out} (p,ρ) [kJ/kg]		
Run 1	71.1	0.522	−332	−52.5	−302	−2,050	0.73%
Run 2	70.8	0.409	−332	−51.8	−301	−2,080	0.58%
Run 3	74.0	1.23	−337	−49.8	−292	−2,760	1.7%

NOTE: Despite the velocity is not included in the table, the kinetic energy was considered for the calculations.

experimentally measured pressure, flow rate and density values at the primary inlet and ejector outlet, along with the measured pressure and temperature values at the secondary inlet. The results are summarized in Table 2. It can be seen that ΔE corresponds to approximately 10% (~2 kW) of the total rate of energy at the primary inlet for the three runs. This result can be most likely explained by the propagation of the measurement error since the ejector wall was thermally insulated.

The experimental ER obtained was low, below 2%, for all three cases (see Table 2). Significantly higher entrainment ratios would be typically expected when an ejector operates in a double choking regime under near-design conditions. These results are consistent with an ejector flow where only the primary stream is choked in the motive nozzle.

2.4 CFD model development and assumptions

The ejector simulation was performed using FLUENT (ANSYS, United States) assuming steady-state homogeneous two-phase compressible flow. The governing equations considered in the simulations were the mass, momentum, energy, and turbulence equations. The energy equation in FLUENT treats pressure and temperature as independent thermodynamic variables. Therefore, an additional transport equation for phase volume or mass fraction is needed for two-phase flows. To avoid the need for this additional transport equation, the enthalpy-based energy equation was implemented so that specific enthalpy and pressure could be treated as the independent thermodynamic variables, as proposed in Smolka et al. (2013).

The main difference between the current model and the previously published ones lies in the method used to calculate fluid properties. Here, CO_2 properties were incorporated into FLUENT as a real gas by developing a user-defined real gas model (UDRGM). This approach enables the computation of thermodynamic and transport properties based on cell pressure and enthalpy, as shown Equation 2:

$$\rho, T, c_p, \mu, \kappa, c, s = f(p, h). \tag{2}$$

The UDRGM uses a predefined property table, generated for a given range of enthalpy and pressure. The table was generated using the equation of state developed by Span and Wagner (1996) for CO_2. The thermal conductivity was determined using the method proposed by Vesovic et al. (1990), while viscosity was calculated using the approach described by Fenghour et al. (1998).

As mentioned before, the energy equation in Fluent was replaced by a user-defined scalar transport equation for the enthalpy having the following form (Smolka et al., 2013):

$$\nabla \cdot \left(\rho \tilde{u} \tilde{h}\right) - \nabla \cdot \left(\Gamma_{h,eff} \cdot \nabla \tilde{h}\right) = \dot{S}_1 + \dot{S}_2 + \dot{S}_3. \tag{3}$$

In Equation 3, $\Gamma_{h,eff}$ represent the effective enthalpy diffusion coefficient and $\dot{S}_1$, $\dot{S}_2$ and $\dot{S}_3$ denote distinct scalar source terms that describe mechanical energy, irreversible dissipation of kinetic energy variation and turbulent kinetic energy dissipation, respectively. To reduce computational costs, a 2D axisymmetric approach was followed, taking advantage of the ejector geometry that permits this assumption (Song et al., 2020). In this case, the different terms in Equation 3 can be expressed as shown in Equations 4–6:

$$\dot{S}_1 = \left(\frac{\partial \tilde{u}}{\partial x}, \frac{\partial \tilde{v}}{\partial y}\right) \cdot \left(\frac{\partial \bar{p}}{\partial x}, \frac{\partial \bar{p}}{\partial y}\right); \tag{4}$$

$$\dot{S}_2 = (\mu + \mu_T)\left\{2\left[\left(\frac{\partial \tilde{v}}{\partial y}\right)^2 + \left(\frac{\tilde{v}}{y}\right)^2 + \left(\frac{\partial \tilde{u}}{\partial x}\right)^2\right] + \left(\frac{\partial \tilde{v}}{\partial x} + \frac{\partial \tilde{u}}{\partial y}\right)^2 - \frac{2}{3}\left(\frac{\partial \tilde{v}}{\partial y} + \frac{\tilde{v}}{y} + \frac{\partial \tilde{u}}{\partial x}\right)^2\right\} - \frac{2}{3}\bar{\rho}k\left(\frac{\partial \tilde{v}}{\partial y} + \frac{\tilde{v}}{y} + \frac{\partial \tilde{u}}{\partial x}\right); \tag{5}$$

$$\dot{S}_3 = -\bar{\rho}\left(\frac{\partial \tilde{u}}{\partial x}, \frac{\partial \tilde{v}}{\partial y}\right) \cdot \nabla k. \tag{6}$$

In addition to assuming thermodynamic and mechanical equilibrium (HEM approach), the ejector walls were considered adiabatic with a no-slip condition. The turbulence model employed was the k-ω SST (Lucas et al., 2014).

The simulation domain is presented in Figure 6, where each boundary condition is identified. The boundary condition type for the primary inlet was specified as pressure-inlet based on the analysis conducted on the experimental data in Section 2.3. The pressure and enthalpy values were determined using the experimentally measured data, with the pressure directly read from the sensors and the enthalpy calculated based on the measured pressure and density. The specific primary flow inlet boundary conditions can be found in Table 3. For the ejector outlet, the pressure boundary conditions were applied considering the measured pressures as indicated in Table 1. Other variables such as temperature, density and enthalpy were computed outputs.

Considering the experimental setup, it is important to note that the recorded entrained mass flow rates did not necessarily correspond to the maximum achievable values under critical conditions. This means that the flow inside the ejector might not be operating at the double-choking conditions. To analyse possible

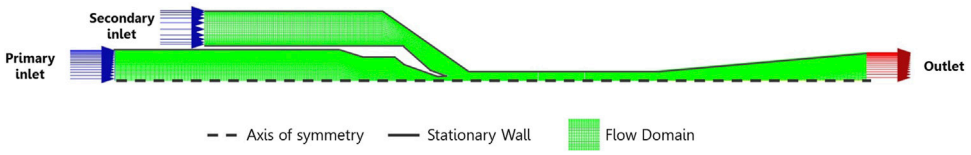

FIGURE 6
Simulation domain, with different boundary layers identified. Details about fluid properties for inlets and outlets can be found on Table 3.

TABLE 3 Boundary conditions for the ejector flow, experimental and CFD predicted motive and entrained mass flow rate [g/s], secondary static pressure [kPa] and density at ejector outlet [kg/m^3] and entrainment ratio. The CFD results are presented in bold.

		Motive nozzle inlet (pr)				Suction chamber inlet (sec)						Ejector outlet (out)		
		p	h* (p,ρ)	$\dot{m}_{pr-CFD}$	$\delta_{\dot{m}_{pr}}$	h* (p,T)	p_{sec}	$\delta_{p_{sec}}$	$\dot{m}_{sec}$	$\delta_{\dot{m}_{sec}}$	ER	p	ρ_{out}	$\delta_{\rho_{out}}$
BC	RUN	[kPa]	[kJ/kg]	[g/s]	[%]	[kJ/kg]	[kPa]	[%]	[g/s]	[%]	[-]	[kPa]	[kg/m3]	[%]
1	1	3,483	−332	**70.0**	−1.5%	−52.5	2,012	—	**11.2**	2049%	0.16	2,233	**258**	−12%
	2	3,474	−332	**69.4**	−2.0%	−51.8	2,013	—	**11.6**	2,744%	0.17	2,227	**249**	−14%
	3	3,451	−334	**69.8**	−5.7%	−49.8	1,732	—	**12.1**	882%	0.17	1,961	**203**	−0.49%
2	1	3,483	−332	**70.0**	−1.5%	−52.5	**1,921**	−4.5%	0.522	—	0.01	2,233	**575**	97%
	2	3,474	−332	**69.4**	−2.0%	−51.8	**1,915**	−4.9%	0.409	—	0.01	2,227	**569**	97%
	3	3,451	−334	**69.8**	−5.7%	−49.8	**1,604**	−7.4%	1.230	—	0.02	1,961	**397**	95%
3	1	3,483	−332	**70.0**	−1.5%	—	**1,912**	−4.9%	0.0	—	—	2,233	**618**	111%
	2	3,474	−332	**69.4**	−2.0%	—	**1,908**	−5.2%	0.0	—	—	2,227	**602**	109%
	3	3,451	−334	**69.8**	−5.7%	—	**1,583**	−8.6%	0.0	—	—	1,961	**455**	124%

operating regimes, three different boundary condition types were considered for the secondary inlet:

- Pressure inlet boundary condition (BC1), with the experimentally measured pressures, was applied to study the double-choking flow regime. The boundary condition for the specific enthalpy was calculated using the pressure and temperature readings. The corresponding values are shown in Table 3;
- Mass flow inlet boundary condition (BC2) was selected to validate flow properties and flow regimes. In this case, applied secondary flow rates are shown in Table 1. For enthalpy, the boundary conditions were the same as in Table 3;
- A third scenario (BC3) was also tested to predict the lowest suction pressure that the ejector could reach. In this case, zero mass and enthalpy flux were applied as BC on the secondary inlet.

The pressure-based steady-state solver was selected for the simulations, utilizing a pressure-velocity couple scheme, with a second-order upwind spatial discretization method for the unknown variables and the Green–Gauss Cell-Based method to evaluate gradients. Convergence was obtained when the relative residuals for the governing equations remained below 10^{-6} and the relative mass flow rate variation over 500 consecutive iterations was less than 0.1%. It is important to note that, from a classical perspective, for highly compressible flows with the existence of shock waves, density-based solvers are often more recommended. However, recent studies (Yazdani et al., 2012; Smolka et al., 2013; Lucas et al., 2014; Giacomelli et al., 2018; Haida et al., 2018; Giacomelli, 2019; Tashtoush et al., 2019; Majchrzyk et al., 2022) have demonstrated the pressure-based solver's capability to accurately resolve the ejector flow.

The structured numerical mesh used in this study consisted of quadrilateral control volumes. A mesh sensitivity analysis was performed using data from Run 1 and BC1 type boundary conditions for the secondary flow. The analysis involved adjusting the mesh density along radial and axial directions, as well as adjusting the boundary layer resolution. Numerical meshes with control volumes ranging from 35,670 to 107,010 were tested. The mesh independence criteria were set based on motive and suction mass flow predictions. Additionally, it was observed that achieving a $y^+ \approx 1$, required for the SST k-ω turbulence model (ANSYS Inc, 2013), presented numerical convergence challenges. As a result, a mesh configuration of 71,340 cells was selected for the remaining simulations. This mesh led to somewhat higher y^+ values (<55) in the ejector nozzle throat, which turned the SST k-ω model to be identical to the standard k-ε model in these locations near the

wall. Additionally, y^+ did not present a significant impact on the flow rates. The maximum relative difference for the motive and entrained mass flow rates were 0.03% and 2% when the results with the selected mesh were compared to a mesh with $y^+<2$. Is also noted that FLUENT provides a well calibrated y^+ insensitive wall treatment for turbulence models based on the ω-equation (ANSYS, 2021). This treatment blends the viscous sublayer formulation and the logarithmic layer formulation based on y^+, ensuring continuous solutions near the wall, despite the variations in y^+.

3 Results and discussion

3.1 Flow rate and density analysis

Table 3 summarizes the computed motive mass flow rates in comparison to the experimental data, indicating the deviation between the results for each tested condition. The predicted mass flow rate for the motive flow is independent of the secondary inlet boundary condition, thus only one set of results is shown here for each run. The model accurately estimated the experimental motive mass flow rates, with a maximum and average relative error of 5.7% and 3.1%, respectively. It is worth noting that these deviations are considerably lower than what is typically reported in the literature for HEM predictions. Previous studies (Palacz et al., 2015; Haida et al., 2018) have shown that the accuracy of HEM in predicting the motive mass flow rate significantly decreases for inlet pressures below 5.9 MPa (around −33%), which is the case in this study. Unfortunately, no published data were found for CO_2 ejectors considering a primary inlet pressure as low as 3.4 MPa, making direct comparisons challenging.

The experimental and predicted entrained flow rates, for double choking operation (BC1), are shown in Table 3. The discrepancy between the measured and CFD simulations was found to be extremely large, with the simulated $\dot{m}_{sec}$ being approximately 20 times higher than the measured values. This discrepancy largely exceeds any expected range, which is typically within a relative error of 20%–40% based on published validation data (Smolka et al., 2013; Palacz et al., 2015). These results suggest that the experimental measurements were not carried out under double choked ejector flow conditions, but rather in single choked regime.

The CFD results for the entrainment ratio (ER) with BC1 are also presented in Table 3. The CFD simulations resulted in ER values of about 0.17. In comparison, the experimental data presented in (Smolka et al., 2013; Palacz et al., 2015), for an equivalent compression ratio of 1.1 (the ratio between the outlet and secondary inlet pressures) showed an ER range of about 0.24–0.67, slightly higher than the values predicted by the current model.

The fluid density and pressure directly determine the vapour quality in a two-phase ejector simulation. The ejector outlet density is influenced by the entrainment ratio, and it is expected that a higher ER would result in a lower outlet density, assuming the inlet and outlet conditions remain unchanged for a flashing ejector. Therefore, one would anticipate that the CFD-predicted CO_2 outlet density for BC1 would be significantly lower than the experimental results. However, the obtained results show a relatively good agreement for the density, with an average error of 8.6% (maximum error 13.6%). To further investigate the discrepancy between the simulated and measured data, the CFD model was run with the measured flow rates imposed on the suction side (BC2). The predicted outlet density results and the corresponding errors are presented in Table 3. For Run 1, the results indicated that the outlet CO_2 density increased from 258 kg/m^3 (under BC1) to 575 kg/m^3 (under BC2) when the secondary mass flow rate decreased. This value is almost twice as high as the experimental data. This result alone would suggest a flow condition that is nearly double-choked inside the ejector for which the secondary mass flow rate should have a considerably higher value than the observed.

3.2 Pressure profile assessment

Since it was not possible to fully validate the CFD simulations with the experimental data under the double choking regime assumption, simulations were performed with the experimentally measured secondary flow rates as boundary conditions (BC2) to calculate the corresponding inlet pressures. Additionally, simulations were also performed with no secondary flow (BC3), to determine the lowest possible suction (secondary inlet) pressures that the ejector could reach. These results were compared with the experimental data for each test run as shown in Table 3. It is clear from the table that using the BC3, the CFD simulations underestimated the experimental secondary inlet pressure values for all test runs. The deviations varied between 5% and 9%, being the highest for Run 3, in which case the experimentally recorded secondary mass flow rate was also the largest. Comparing the results between applying BC2 and BC3, one may note that there was little variation between the predicted secondary inlet pressures. This is because the experimental flow rates were already very small, thus assuming zero flow rate (BC3) had little impact on the predicted inlet pressure. In general terms however, it can be stated that using the experimentally recorded suction flow rates as boundary conditions, a good agreement between the CFD model and the experimental results was obtained for the secondary inlet pressure.

The simulated pressure profiles along the ejector wall in the constant area section and diffuser are shown in Figure 7, where the axial position (x) is measured from the constant area section inlet. The experimental pressure data is shown for the constant area section, with an error estimate of ± 2% from the measured values. Looking at the figure, it is evident that the CFD simulations underestimated the wall static pressure in the constant area section when considering a double-choked ejector flow (BC1). Additionally, the shape of the pressure distribution profile differed from that obtained with BC2 and BC3. Specifically, BC1 exhibited lower wall pressure values in the constant area section. This observation agrees with expectations, as BC1 involves an entrained flow at low pressure. In the initial part of the constant area section ($x < 8.2$ mm), before mixing the two streams (primary and secondary), considerably lower pressures were observed, mainly corresponding to the secondary stream pressure. Further downstream, the pressure starts to increase, suggesting the beginning of the mixing process and culminating in a shock wave at the diffuser inlet.

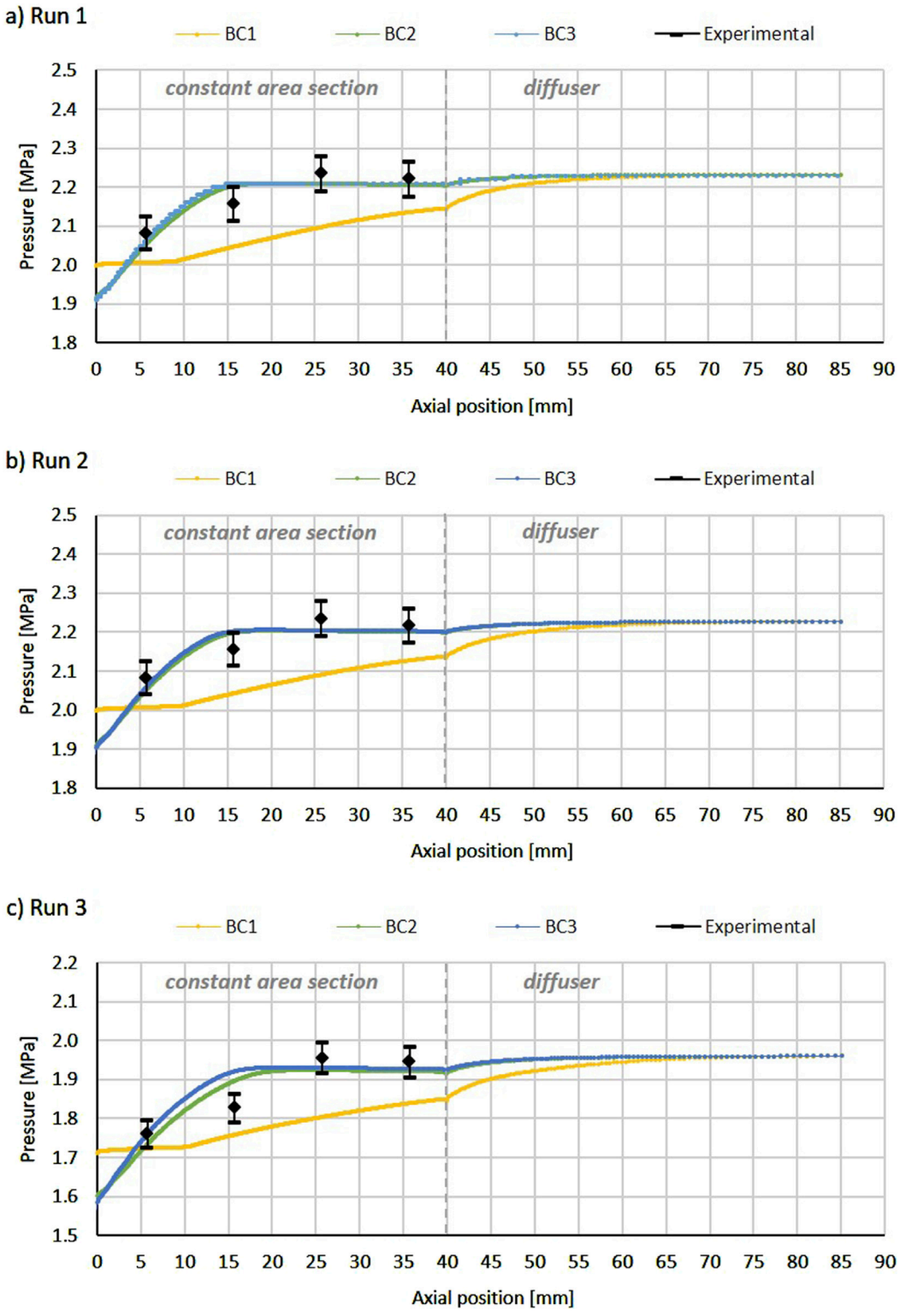

FIGURE 7
Experimental wall pressure profile for the constant area section and CFD results for the constant area section and diffuser, for Run 1 **(A)**, Run 2 **(B)** and Run 3 **(C)**.

Analysing the simulation results for BC2 (experimental entrained flow as input) and BC3 (no entrained flow), it is obvious that Run 1 and 2 resulted in similar wall pressure distributions regardless BC2 or BC3 was applied. This similarity can be attributed to the very low measured secondary flow rates in both cases. However, for Run 3, applying BC2 resulted in slightly lower wall pressures in the initial part of the constant area section. This observation indicates that the existence of a secondary flow rate

had a significant impact on the pressure profile (such as in the case for BC1).

When comparing the simulation results with the experimental data, it was observed that the model-predicted wall pressure distribution fell within the estimated experimental error range. This indicates a good overall accuracy of the CFD model. However, it also suggests that the ejector operated off-design mode during the experiments, without reaching its optimal performance. A relatively larger deviation of 5% was observed for Run 3 at point 2. This discrepancy can be explained by the limitations of the applied RANS model, which does not accurately capture the intensity and location of the shock train that occurs at the nozzle outlet. In general, the CFD predictions of wall static pressure were in good agreement with the experimental data. The average error, considering BC2, was approximately −0.6% with a standard deviation of 1.9% for the three runs.

3.3 Temperature profile assessment

The experimental temperature profiles, measured at seven different axial positions, were compared to the simulated ones, considering the experimental uncertainty of ± 0.4 K. These points with their corresponding uncertainty are shown in Table 3, together with the simulation results. It should be noted that the exact radial location of the measurement points was not accurately known. Using BC1, there was a significant radial temperature variation (between 9°C and 24°C) at the entrance of the constant area, which caused large fluctuations in the average temperature profile, as shown in Table 3. This is because the mixing process has not yet started, and there were differences in state properties between the primary and secondary jets. Mixing started at about x = 8.2 mm for Run 1 and 2, and at x = 10 mm for Run 3. Downstream these locations, the temperature profile fluctuation is caused by the generated shock waves.

Approximately at an axial position of 25 mm (similar for all the runs), the simulated temperature distribution became more uniform across the ejector section, indicating the completion of the mixing process. Runs 1 and 2 (Figures 8A, B) yielded very similar results due to the similar test conditions. However, in Run 3 (see Figure 8C), the inlet pressure and temperature for the entrained flow were lower, while the differences in motive flow properties were not as significant. Additionally, the outlet pressure in Run 3 was lower, resulting in a higher entrained flow rate. This could explain the delay in the mixing process and why the oscillation in the temperature profile decreased. Nevertheless, the CFD predictions indicated that the mixing process was completed at a similar axial position for all runs.

The temperature profiles obtained for BC2 and BC3 were similar, resulting in overlapping curves in Figure 8. However, when comparing the results for BC2 (or 3) to BC1 in the constant area section, there is a noticeable difference. Since BC2 imposes a very low entrained mass flow rate, the mixing effects are negligible. Therefore, the motive stream behaved like a free supersonic jet undergoing a series of oblique shock waves. Using BC2, the temperature increased rapidly approximating the outflow temperature, still inside the constant area section. The sudden change in the cross-sectional area at the diffuser slightly increased the stream pressure and therefore temperature.

When comparing the experimental and CFD data applying BC1, it was observed that the measured flow temperature fell within the temperature range predicted by the CFD for the first two axial measurement sections in Runs 1 and 2. The largest prediction error was observed at point 3 for these cases and at point 2 for Run 3. However, this difference gradually reduced and became insignificant as the flow entered the diffuser. In the diffuser section, the simulated flow temperatures were uniform for all three runs, indicating excellent agreement with the measured data.

Regarding BC2, the average temperature inside the ejector showed a 7°C difference between the experimental data and prediction. However, the experimentally recorded temperature data fell within the predicted temperature range at the same axial location (cross-section). For the remaining points, the experimental temperature was consistent with the predicted temperatures with BC2 (and BC3). This demonstrates that the experimental results are consistent with very low secondary flow rate conditions.

Table 4 summarizes the ejector outlet temperatures (T_{out}) obtained experimentally from simulation by calculating the mass-weighted average data ($T_{out\text{-}CFD}$) and obtained assuming saturation (T^*_{out}) from the two-phase outflow condition. The saturation temperature was calculated using the CO_2 property table for the measured p_{out}. It is important to note that the simulated outlet temperatures were not affected by the applied boundary conditions (BC1–3). This is because the ejector outflow is at wet vapour state, and the outlet pressure was the same for all three different boundary conditions. Therefore, any fluctuations in $\dot{m}_{sec}$ would only impact the vapour quality at the ejector exit. Due to this reason, the differences between the CFD simulated outlet temperatures ($T_{out\text{-}CFD}$) and the T^*_{out}, were negligible. However, when comparing $T_{out\text{-}CFD}$ with T_{out}, the differences ranged between 7°C and 10°C. This deviation is significantly higher than what would be expected considering a reasonable level of measurement error for the temperature sensors. It is suspected that T_{out} was not accurately determined during the experiment, as it was measured on the pipeline wall. This suspicion is supported by the data in Table 4. The last temperature sensor inside the ejector (7) near the exit (see Figure 5) recorded temperatures close to the simulated data and the values were calculated assuming saturation conditions. The temperature variation inside the ejector remained within 5°C for all test runs, suggesting that the significantly lower temperature reading towards the ejector outlet may have resulted from measurement error. Therefore, it was concluded that the CFD simulations accurately predicted the temperature profile.

3.4 Energy balance analysis

The results of applying the ejector energy balance (Equation 1) to the CFD data are shown in Table 5. As expected, the CFD simulation results showed a negligible mismatch between inlets and outlets, in agreement with the adiabatic wall assumption. This small difference was primarily attributed to numerical errors. When calculating the energy balance for the experimentally recorded data, a discrepancy of approximately 2 kW between the rate of energy entering and exiting the ejector (Table 2). Furthermore, if the energy balance were calculated using the enthalpies resulting from the experimental conditions and incorporating the simulated

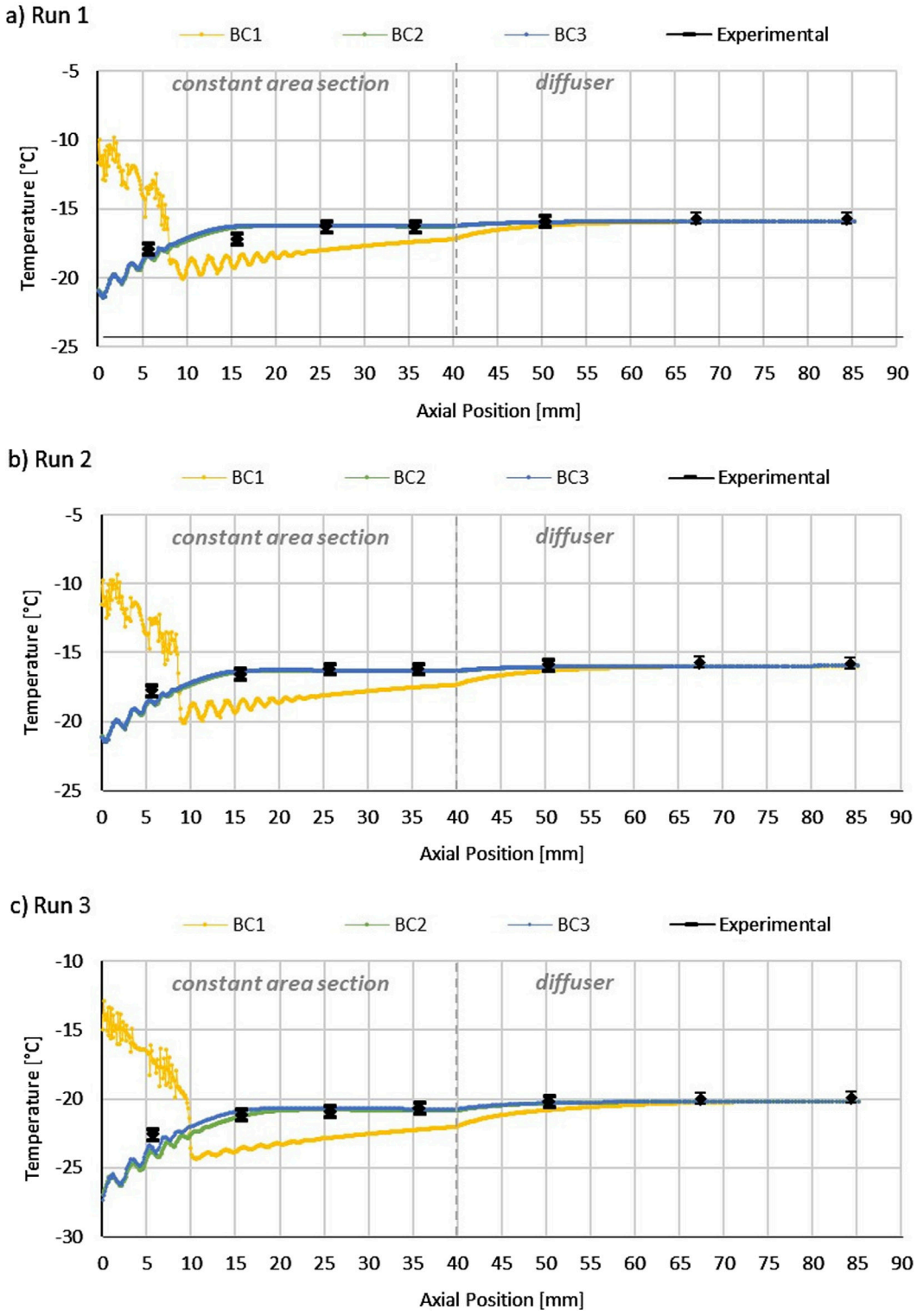

FIGURE 8
Temperature distribution, after the nozzle outlet, simulated by the CFD model and obtained by experimental measurements (with the corresponding error bars): **(A)** Run 1, **(B)** Run 2 and **(C)** Run 3.

secondary mass flow rates with BC1, an average energy imbalance of −2.5 W would have been obtained. This also suggests that the experimental data may have been influenced by relatively significant measurement errors.

4 Conclusion

This study aimed to comprehensively assess the predictive capabilities of a two-phase flow CFD model using HEM, for a

TABLE 4 Temperature profile along the ejector length for the three test runs and outlet ejector temperature comparison between experimental (Tout), estimated by EES (T*out) and the mass-weighted average temperature at the ejector outlet predicted by CFD (Tout-CFD).

	Constant area section				Diffuser			Ejector outlet			
	1	2	3	4	5	6	7	T_{out}	T^*_{out}	$T_{out\text{-}CFD}$	$T_{out}-T^*_{out}$
Run 1	−17.9	−17.2	−16.3	−16.3	−15.9	−15.7	−15.7	−8.9	−15.9	−15.9	6.9
Run 2	−17.7	−16.6	−16.2	−16.2	−15.9	−15.7	−15.8	−8.4	−16.0	−16.0	7.6
Run 3	−22.6	−21.2	−20.9	−20.7	−20.2	−20.0	−19.9	−10.3	−20.2	−20.2	9.8

TABLE 5 Energy imbalance properties and results.

		CFD						Experimental
		$\dot{m}_{pr}$ [g/s]	h^*_{pr} [kJ/kg]	$\dot{m}_{sec}$ [g/s]	h^*_{sec} [kJ/kg]	h_{out} [kJ/kg]	ΔE [W]	ΔE [W]
Run 1	BC1	70.0	−332	11.2	−52.5	−294	3.46	−2,050
	BC2			0.522	−52.5	−330	0.876	
	BC3			0	−333	−332	1.04	
Run 2	BC1	69.4	−332	11.6	−51.8	−292	3.44	−2,080
	BC2			0.409	−51.8	−330	0.945	
	BC3			0	−332	−332	1.09	
Run 3	BC1	69.8	−334	12.1	−49.8	−292	4.90	−2,760
	BC2			1.23	−49.8	−329	0.400	
	BC3			0	−34.1	−334	0.47	

flashing CO_2 ejector operating with a reduced pressure of 0.47 at the motive flow inlet. The work also demonstrated how CFD simulations can be applied to critically explore experimental data and to identify potential issues with the results. The main conclusions of this study can be summarized as follows:

1. The CFD model accurately predicted the motive mass flow rate (maximum error of 5.7%) and outflow density (maximum error of 13.6%) assuming double choking condition, demonstrating its capability to capture the overall flow behaviour.
2. The simulated entrained mass flow rates and entrainment ratios were unexpectedly higher (in some cases twenty times) than the experimental values, indicating a discrepancy between the model assumptions (boundary conditions) and the actual flow behaviour during the mixing process. This discrepancy is significantly larger than what was anticipated based on published data.
3. The comparison of the different boundary conditions for the secondary inlet revealed that the deviations in simulated ejector outlet properties increased significantly for the imposed secondary inlet flow rate (from a maximum error of 13.6%, for double choke condition, to nearly 100%). This could suggest double choked flow during the experiment, which is not consistent with the other results, such as the pressure and temperature profiles at the ejector wall.
4. When considering the experimental entrained flow rate, a significant discrepancy was observed in the outflow density compared to the experimental data (around 100% error). However, the pressure (deviations varied between 0.6% and 3.3%) and temperature (difference between experimental and CFD varied between −2.1°C and 0.8°C) distributions along the ejector length were accurately predicted by the CFD model. This observation supports the notion of a single choked flow regime during the experimental work.
5. The analysis of the pressure profile showed consistent underestimation by the CFD model, while the shape of the pressure distribution differed from the experimental results. This discrepancy can be attributed to the limitations of the applied RANS model in accurately capturing the interaction between the mixing jets.
6. The temperature profile analysis supported the experimental observation of a very low secondary flow rate during the experiment.
7. The energy balance analysis indicated a 2 kW discrepancy, suggesting relatively high experimental errors, probably associated with the secondary flow measurements.

The results showed the limitation of the applied CFD model to accurately predict two-phase flashing ejector flow. Some of these limitations cannot be explained by inadequate assumptions and applied boundary conditions only. Therefore, further research is

needed to generate high-quality experimental data and make them available for CO_2 ejector model validation. This data could be then used to improve CFD prediction accuracy and gather a better understanding of the ejector's flow behaviour under different operating conditions.

Data availability statement

The original contributions presented in the study are included in the article/supplementary material, further inquiries can be directed to the corresponding author.

Author contributions

KG: Conceptualization, Investigation, Methodology, Software, Writing–original draft. SV: Investigation, Resources, Supervision, Writing–review and editing. DB: Methodology, Resources, Writing–review and editing. KŚ: Methodology, Resources, Writing–review and editing.

Funding

The author(s) declare that financial support was received for the research, authorship, and/or publication of this article. This work was supported by the Foundation for Science and Technology (FCT) and the Associate Laboratory for Energy, Transports and Aerospace (LAETA) through the grant UI/BD/150846/2021.

Acknowledgments

The authors would like to acknowledge the Foundation for Science and Technology (FCT) and the Associate Laboratory for Energy, Transports and Aerospace (LAETA) for the financial support of this work through grant contracts with reference UI/BD/150846/2021.

Conflict of interest

The authors declare that the research was conducted in the absence of any commercial or financial relationships that could be construed as a potential conflict of interest.

Publisher's note

Supplementary material

The Supplementary Material for this article can be found online at: https://www.frontiersin.org/articles/10.3389/fmech.2024.1410743/full#supplementary-material

References

Angielczyk, W., Seynhaeve, J. M., Gagan, J., Bartosiewicz, Y., and Butrymowicz, D. (2019). Prediction of critical mass rate of flashing carbon dioxide flow in convergent-divergent nozzle. *Chem. Eng. Process. Process Intensif.* 143 (2), 107599. doi:10.1016/j.cep.2019.107599

ANSYS (2021). "ANSYS fluent theory guide."

ANSYS Inc (2013). "ANSYS fluent user's guide." 15.0.

Banasiak, K., and Hafner, A. (2011). 1D computational model of a two-phase R744 ejector for expansion work recovery. *Int. J. Therm. Sci.* 50 (11), 2235–2247. doi:10.1016/j.ijthermalsci.2011.06.007

Bodys, J., Smolka, J., Palacz, M., Haida, M., Banasiak, K., and Nowak, A. J. (2022). Effect of turbulence models and cavitation intensity on the motive and suction nozzle mass flow rate prediction during a non-equilibrium expansion process in the CO2 ejector. *Appl. Therm. Eng.* 201, 117743. doi:10.1016/j.applthermaleng.2021.117743

Colarossi, M., Trask, N., Schmidt, D. P., and Bergander, M. J. (2012). Multidimensional modeling of condensing two-phase ejector flow. *Int. J. Refrig.* 35, 290–299. doi:10.1016/j.ijrefrig.2011.08.013

Fang, Y., Poncet, S., Nesreddine, H., and Bartosiewicz, Y. (2019). An open-source density-based solver for two-phase CO2 compressible flows: verification and validation. *Int. J. Refrig.* 106, 526–538. doi:10.1016/j.ijrefrig.2019.05.016

Fenghour, A., Wakeham, W. A., and Vesovic, V. (1998). The viscosity of carbon dioxide. *J. Phys. Chem. Reference Data* 27 (1), 31–44. doi:10.1063/1.556013

Giacomelli, F. (2019). *Numerical modeling of supersonic two-phase ejectors working with natural refrigerants*. Italy: Univerity of Florence.

Giacomelli, F., Banasiak, K., Hafner, A., Mazzelli, F., and Milazzo, A. (2018). Experimental and numerical investigation on an ejector for CO2 vapor compression systems. *Refrig. Sci. Technol. 2018-June*. doi:10.18462/iir.gl.2018.1392

Giacomelli, F., Mazzelli, F., Banasiak, K., Hafner, A., and Milazzo, A. (2019). Experimental and computational analysis of a R744 flashing ejector. *Int. J. Refrig.* 107, 326–343. doi:10.1016/j.ijrefrig.2019.08.007

Haida, M., Smolka, J., Hafner, A., Palacz, M., Banasiak, K., and Nowak, A. J. (2018). Modified homogeneous relaxation model for the R744 trans-critical flow in a two-phase ejector. *Int. J. Refrig.* 85, 314–333. doi:10.1016/j.ijrefrig.2017.10.010

Hassanain, M., Elgendy, E., and Fatouh, M. (2015). Ejector expansion refrigeration system: ejector design and performance evaluation. *Int. J. Refrig.* 58, 1–13. doi:10.1016/j.ijrefrig.2015.05.018

Huang, H., Huang, J., Lu, X.-Y., and Sukop, M. (2013). On simulations of high-density ratio flows using color-gradient multiphase Lattice Boltzmann models. *Int. J. Mod. Phys. C* 24 (04), 1350021. doi:10.1142/S0129183113500216

Ishii, M., and Hibiki, T. (2006). *Thermo-fluid dynamics of two-phase flow*. 1st ed. Boston, MA: Springer US. doi:10.1007/978-0-387-29187-1

Liu, G., Wang, Z., Zhao, H., and Abdulwahid, A. A. (2022). R744 ejector simulation based on homogeneous equilibrium model and its application in trans-critical refrigeration system. *Appl. Therm. Eng.* 201, 117791. doi:10.1016/j.applthermaleng.2021.117791

Lucas, C., Rusche, H., Schroeder, A., and Koehler, J. (2014). Numerical investigation of a two-phase CO2 ejector. *Int. J. Refrig.* 43, 154–166. doi:10.1016/j.ijrefrig.2014.03.003

Majchrzyk, M., Dziurowicz, D., Haida, M., Palacz, M., Bodys, J., Fingas, R., et al. (2022). Detailed numerical investigation of the CO2 two-phase ejector 3-D CFD model based on the flow visualisation experiments. *Chem. Eng. Process. - Process Intensif.* 182, 109195. doi:10.1016/j.cep.2022.109195

Noori, S. M. S., Rahni, M. T., and Taleghani, S. A. S. (2019). Multiple-relaxation time color-gradient Lattice Boltzmann model for simulating contact angle in two-phase flows with high density ratio. *Eur. Phys. J. Plus* 134 (8), 399. doi:10.1140/epjp/i2019-12759-x

Palacz, M., Haida, M., Smolka, J., Nowak, A. J., Banasiak, K., and Hafner, A. (2017). HEM and HRM accuracy comparison for the simulation of CO2 expansion in two-phase ejectors for supermarket refrigeration systems. *Appl. Therm. Eng.* 115, 160–169. doi:10.1016/j.applthermaleng.2016.12.122

Palacz, M., Smolka, J., Fic, A., Buliński, Z., Nowak, A. J., Banasiak, K., et al. (2015). Application range of the HEM approach for CO2 expansion inside two-phase ejectors

for supermarket refrigeration systems. *Int. J. Refrig.* 59, 251–258. doi:10.1016/j.ijrefrig.2015.07.006

Parikhani, T., Delpisheh, M., Haghghi, M. A., Holagh, S. G., and Athari, H. (2021). Performance enhancement and multi-objective optimization of a double-flash binary geothermal power plant. *Energy Nexus* 2, 100012. doi:10.1016/j.nexus.2021.100012

Reddick, C., Sorin, M., Sapoundjiev, H., and Aidoun, Z. (2016). Carbon capture simulation using ejectors for waste heat upgrading. *Energy* 100, 251–261. doi:10.1016/j.energy.2016.01.099

Ringstad, K. E., Allouche, Y., Gullo, P., Ervik, Å., Banasiak, K., and Hafner, A. (2020). A detailed review on CO2 two-phase ejector flow modeling. *Therm. Sci. Eng. Prog.* 20, 100647. doi:10.1016/j.tsep.2020.100647

Ringstad, K. E., and Hafner, A. (2020). "Two-fluid CFD model for R744 two-phase ejectors," in *Refrigeration Science and technology, 2020-decem*, 375–380. doi:10.18462/iir.gl.2020.1147

Sharifi, N., Noori Rahim Abadi, S. M. A., and Kouhikamali, R. (2021). Development of a two-fluid model for predicting phase-changing flows inside thermal vapor compressors used in thermal desalination systems. *Appl. Therm. Eng.* 195, 116943. doi:10.1016/j.applthermaleng.2021.116943

Smolka, J., Buliński, Z., Fic, A., Nowak, A. J., Banasiak, K., and Hafner, A. (2013). A computational model of a transcritical R744 ejector based on a homogeneous real fluid approach. *Appl. Math. Model.* 37 (3), 1208–1224. doi:10.1016/j.apm.2012.03.044

Song, Y., Ma, Y., Wang, H., Yin, X., and Cao, F. (2020). Review on the simulation models of the two-phase-ejector used in the transcritical carbon dioxide systems. *Int. J. Refrig.* 119, 434–447. doi:10.1016/j.ijrefrig.2020.04.029

Span, R., and Wagner, W. (1996). A new equation of state for carbon dioxide covering the fluid region from the triple-point temperature to 1100 K at pressures up to 800 MPa. *J. Phys. Chem. Reference Data* 25 (6), 1509–1596. doi:10.1063/1.555991

Taleghani, A. S., and Noori, M. S. (2022). Numerical investigation of coalescence phenomena, affected by surface acoustic waves. *Eur. Phys. J. Plus* 137 (8), 975. doi:10.1140/epjp/s13360-022-03175-8

Tashtoush, B. M., Al-Nimr, M. A., and Khasawneh, M. A. (2019). A comprehensive review of ejector design, performance, and applications. *Appl. Energy* 240, 138–172. doi:10.1016/j.apenergy.2019.01.185

Vesovic, V., Wakeham, W. A., Olchowy, G. A., Sengers, J. V., Watson, J. T. R., and Millat, J. (1990). The transport properties of carbon dioxide. *J. Phys. Chem. Reference Data* 19 (3), 763–808. doi:10.1063/1.555875

Yazdani, M., Alahyari, A. A., and Radcliff, T. D. (2012). Numerical modeling of two-phase supersonic ejectors for work-recovery applications. *Int. J. Heat Mass Transf.* 55 (21–22), 5744–5753. doi:10.1016/j.ijheatmasstransfer.2012.05.071

Zheng, L., Zhang, Y., Hao, L., Lian, H., Deng, J., and Lu, W. (2022). Modelling, optimization, and experimental studies of refrigeration CO2 ejectors: a review. *Mathematics* 10 (22), 4325. doi:10.3390/math10224325

Nomenclature

Latin symbols

c	Speed of sound (m/s)
c_p	Specific heat capacity [J/(kg K)]
ΔE	Energy balance (J)
ER	Entrainment Ratio
h	Specific enthalpy (J/kg)
k	Turbulent kinetic energy (m^2/s^2)
$\dot{m}$	Mass flow rate (kg/s)
p	Static pressure (Pa)
p_r	Reduced pressure
s	Specific entropy [J/(kg K)]
$\dot{S}_\phi$	Source term in a transport equation for scalar ϕ
T	Temperature (K or °C)
Tr	Reduced temperature
ΔT	Temperature difference (K)
u	Velocity vector (m/s)
u, v, w	Velocity vector components in Cartesian coordinates (m/s)
V	Velocity magnitude (m/s)
x	Vapour quality
x, y, z	Cartesian coordinates (m)
$y+$	Non-dimensional distance from the wall to the first mesh node

Greek symbols

δ	Relative error (%)
κ	Thermal conductivity [W/(m·K)]
μ	Dynamic viscosity [kg/(m s)]
μ_T	Turbulent viscosity [kg/(m s)]
ρ	Density (kg/m^3)
σ	Standard deviation
Γ	Diffusion coefficient (m^2/s)
σ_T	Turbulent Prandtl number
ω	Specific turbulence dissipation rate (s^{-1})

Subscripts

pr	Primary ejector inlet—motive inlet flow
sec	Secondary ejector inlet—entrained flow
out	Ejector outflow
exp	Experimental value
CFD	CFD result

Other symbols

*	Computed values using the property function of EES
$\tilde{n}$	Favre averaged
$\bar{n}$	Reynolds averaged

List of abbreviations

2D	Two-dimensional
BC	Boundary Condition
CFD	Computational Fluid Dynamics
CO2	Carbon Dioxide
EES	Engineering Equation Solve
GWP	Global Warming Potential
HEM	Homogeneous Equilibrium Model
HRM	Homogeneous Relaxation Model
ODP	Ozone Depletion Potential
RANS	Reynolds-Averaged Navier–Stokes
SST	Shear Stress Transport
TFM	Two-Fluid Model
UDRGM	User-Defined Real Gas Model